J. Electr. Comput. Eng. Innovations, 7(1): 47-58, 2019

Journal of Electrical and Computer Engineering Innovations

(JECEI)

Research paper

Hemispherical Vibratory Gyroscope Performance Evaluation and Sensitivity Analysis with Capacitive Excitation

R. Sedaghati[1,*], M. Mahmoudian[2]

[1]*Department of Electrical Engineering, Beyza Branch, Islamic Azad University, Beyza, Iran.*

[2]*Department of Electrical Engineering, Firouzabad Institute of Higher Education, Firouzabad, Iran.*

Article Info

Article History:

Received 27 February 2018

Reviewed 05 April 2018

Revised 30 July 2018

Accepted 27 November 2018

Keywords:

Gyroscopes

HRG

Capacitive excitation

Coriolis force

Sensor

[*]Corresponding Author's Email Address:

sedaghati.r@biau.ac.ir

Abstract

Background and Objectives: Coriolis vibratory gyroscope is one of the most modern types of gyroscopes that has been substituted for the common gyroscopes with some differences in the test mass design and elastic suspension. According to the important features observed in the capacitive excitation of the actuators regarding the piezoelectric actuators, the operation principles and their formulations are completely changed, which require both two dimensional and finite element analysis to evaluate their optimal performance. Because the sensors are usually vibrating continuously while operation.

Methods: In this paper a general framework is presented that fully describes the influence of the parameters related to different frequency operating modes. The main idea of the vibration gyroscope is to replace the rotational rotor with a vibrational structure to utilize the effects of Coriolis force, which causes the secondary motion of a sensitive mass to match an angular velocity.

Results: In this paper, the sensitivity analysis and performance evaluation of a hemispherical vibrational gyroscope are discussed. The frequency split phenomenon, the sensed voltage around the resonance frequency and Young's modulus variation are also investigated.

Conclusion: Finally, the results of the simulated resonance frequencies are compared and validated with the mathematical and theoretical principles.

©2019 JECEI. All rights reserved.

Introduction

Vibratory gyroscopes are single-axis or bi-axial scaled gyroscopes that are built with semiconductor technology and integrated lumped circuits. Structurally, they include some chips with a quartz sub-layer of dimensions ranging from a few millimeters to a micron, which is provided by photolithography and similar methods as plate vibrating structures [1]. Due to the impossibility of using bearing structures and engines for the classical gyroscope types (because of their small size), the gyroscopes with this technology use vibrational structures with resilient elastic supports with two resuscitators. The common aspect of this classification of the gyroscope is the use of the motion size of the sensitive element and the Coriolis force to detect the angular velocity of the base of the gyroscope carrier [2]-[3]. In recent years, much attention has been paid to gyroscopes, and many scientific and technical works have been carried out by researchers 0-[7]. What has attracted widespread attention to Coriolis vibratory gyroscope (CVG) is not only the achievement of better accuracy and aerospace applications, but also its extremely low price, and the subsequent dimensionality and small size, which can be very important [8].

Some of the important benefits of these gyroscopes, which have led the researchers in the field of missile and aerospace to operate these gyroscopes in their field of work, are [9]-[11]:

1. They have a short start up time.
2. Due to a lack of rotor axle, they need no bearings.
3. No need for an engine.
4. In the case of effective design, they have a very long lifespan and do not require maintenance or repair.
5. They are much smaller and lighter than traditional gyroscopes.
6. Being Cheap is the most important advantage of these gyroscopes.
7. Comparatively easier to make.
8. A very small energy consumption.

As mentioned, CVGs have many advantages, including low cost, small size, and insignificant weight compared to microscopic gyroscopes. This gyroscope is the main member of the inertial guidance systems and is mainly used to measure the amount of time, velocity, and reference axes in aerial, spatial, marine and terrestrial vehicles. The research target in many research groups is to produce structures measuring from one to five centimeters. Therefore, the problem that designers face is flight stability. Large flying equipment (such as an airplane) is aerodynamically stable and, due to its large size, it is possible to take advantage of positioning systems; however, when a small flying mechanism is required to be stopped (similar to a helicopter fly, but much smaller) this characteristic loses its effectiveness [12]-[13]. In 1851, Peter Foucault showed a swinging pendulum of earth self-motion. Foucault's pendulum can be considered as the prototype of vibrational gyroscopes [14]. In 1964, few researchers provided an analytical investigation of the vibrating curve as an angular motion sensor. The steady flow of the head and the longitudinal motion of the other side stimulated the vibration of the first mode. Authors in [15] represented that if the backbone starts to rotate around the axis, the vibration screen will remain constant. In this paper, they examined the stability conditions, the effects of defects, asymmetry of attenuation and elasticity, but did not provide any practical explanation or laboratory results. This design, like Foucault's Pendulum, was a time angle detector. In the early 1980s, the first set of vibrational gyroscopes was constructed based on angular velocity determination [16]. In this sample, the piezoelectric quartz material was used which has a high efficiency and high coefficient of atmospheric pressure. Also, in 1991, the 'Japanese company Murata' offered two very low-cost designs [17]. They used a triangular cross-sectional steel beam pattern, stimulated and sensed by piezoelectric elements connected to the beams of the source. The second resonator was also considered a piezoelectric quadrilateral beam in which in both designs, the resonators in the first vibrational mode vibrated, like a freewheel, with the supports on the knot points. Gyroscopic designs based on resonators of tar, vibrating beam and pendulum are sensitive to linear accelerations. If a symmetrical resonator such as tuning fork is used, the defect is eliminated. The first projection of the vibrator was presented by Bashestin [18]. In this design, the Coriolis forces caused by the period of the tentacled antennae around the longitudinal axis of tuning fork leads to a torsional oscillation of the base, which is proportional to the amplitude of the applied angular velocity. The design was costly and bulky, and perhaps the main reason behind the inadequacies of the early designs of vibrational gyroscopes could be the same issue, which was solved by using microprocessor processes and minimizing their dimensions. The main step in this area was taken by the Sistron Duner company [19]. In the company's design, a quartz dash was used which was a piezoelectric material (quartz single crystal). The first two branches had different oscillatory movements. Under the influence of the time, the Coriolis force produced a torsional trunk in the base of the diaphragm. As a result, the other two diagonal branches were applied to the base of the torsion and proportional to the angular velocity, but with different natural frequencies, vibrate outside the plate. In the same year, Dapper corporation introduced a silicon-vibration resonator, which was electrically step-less to a range of 10 μm [20]. Correspondingly, the samples with high vibration amplitude and electromagnetic stimulation mechanism are presented. In the automotive industry, Daimler-Benz company, using a piezoelectric stimulation system, which was recycled to put a thin layer of aluminum nitride on the antennae, measured the shear stress induced by the tuning fork base as piezoelectric as the output [21]. An example of tuning fork resonators was also provided by the Sooderwist company, which uses a single-socket disconnector without the usage of a torsion base [22]. The use of shell resonators has also increased dramatically. The vibration analysis and the effect of the period on this category of cylindrical resonators were the basis of General Motors company's work for the successful design of a vibrating gyroscope with a hemisphere resonator [23]. The semiconductor material of this resonator was made of welded quartz, which was electrically stimulated and sensitized. Many patents have been registered on this basis. The hemispherical resonator gyroscope (HRG) technology, with its low cost and volume and high efficiency, made it possible to compete with the precision of beam gyroscopes. A cylindrical vibratory gyroscope (CVG) is another resonator that comes from Brian's idea [24]. In this type, a thin-headed, cylindrical steel cylinder with separate piezoelectric elements is used for sensation and stimulation. The initial application of the plan was based on intelligent missiles and bombs, which proved the ability of this sensor to test the shock to the 25000 *g*. Its first commercial application can be found in the Formula one rally car racing, 1987. In new samples, instead of joining the piezoelectric elements, the piezoelectric material is constructed to the entire cylindrical surface of the device. The British airways company has provided an example of it with two newer designs based on annular resonators [25]-[26]. In this design, the electromagnetic excitation system and the sensor system are capacitive. But in the second plan, both systems are electromagnetic. Today, technology is focused on reducing the cost of producing this category of gyroscopes. Later, the first silicone microscopic gyroscopes were proposed [27].

In this paper, the governing equations for an HRG will be presented in two-dimensional and three-dimensional coordinates.

Then, the sensitivity analysis of the effective parameters changing for an optimal HRG is analyzed, which indicates that frequency modes can have a significant effect on the HRG function.

The finite element analysis of HRG also states that the voltage sensed by the sensor will be around the instantaneous peak oscillation frequencies.

Therefore, the optimal design of the frequency split phenomenon and unwanted resonances at the edge of the resonator can be avoided.

Table 1 demonstrates the superiority of the proposed technology compared with the existing methods.

Table 1: Variable capacitance, piezoresistive, and piezoelectric technology comparison

	Piezo-Electric	Piezo-Resistive	Variable Capacitance (VC)
Operation frequency	3 Hz – 30 kHz	0 – 6 kHz	0 – 6 kHz
Acceleration	Up to 20000 *g*	Up to 2000 *g*	1 to 200 *g*
Operation temperature	-200 to 700 (^{o}C)	-55 to 125 (^{o}C)	-55 to 175 (^{o}C)
SNR	Excellent	good	Excellent
Measured accuracy	10 %	10 %	0.1 %
Stability	Sensitive to temperature	Sensitive to temperature	Stable
Self-test	No self-test	No self-test	True internal self-test

Problem Concept

The basis of all vibrational gyroscopes is the effect of Coriolis force and acceleration. Vibrating gyroscopes have non-rotating components, which are influenced by the effect of accelerated Coriolis to determine the angular momentum of inertia. The acceleration of the Coriolis, which appears due to the rotation of the reference coordinate system, is an acceleration used to describe the rotational motion of the reference machine and the calculation of axial motion. The effect of Coriolis can be seen on many phenomena that have a complex era, including airflow above the earth's surface in the northern and southern hemispheres. To better understand this effect, consider the particle in Fig. 1, which moves along the y-axis at constant velocity $\vec{v}$, and the observer on the x-axis looks at it. As shown in the picture, the observer on the x-axis system is placed in Cartesian coordinates. If, in a given coordinate system, In recent years micro-gyroscopes have been able to reach a commercial level [28], but research on their optimal performance is still ongoing.

the z-axis is rotated at an angular velocity Ω, the observer will realize that the particle changes direction relative to the x-axis with an acceleration equal to $\vec{v} \times 2\vec{\Omega}$. The force generated by this acceleration appears on the third axis, which includes the axis of the rotation and the velocity vector of the particle. It is perpendicular to them and its value is proportional to the angular velocity of the z-axis. However, in this case, the actual force has not been applied to the particle, but from the observer's point of view, the period of the reference system creates an apparent force that is directly proportional to the velocity of the rotation. This principle is based on the operation of vibrating gyroscopes with different types of resonators.

Finally, the Coriolis force is obtained using equation 1.

$$\vec{F} = 2m\vec{\Omega} \times \vec{v} \tag{1}$$

where m is the mass of the sensitive element, $v^{\rightarrow}$ is the velocity of the sensitive element and Ω is the angular velocity measured. Since the Coriolis force is proportional to the velocity, a better sensitivity can be obtained by increasing the trigger velocity of the sensitive element. But as noted in the previous sections, HRGs can measure the angular velocity of the input while its location changes using the effects of Coriolis force. The circular part of the spherical shell of the resonator, repeatedly during the vibration, repeats the movements of the circular-elliptical horizontal and circular-vertical ellipse. The location of the maximum domain and the location of the non-portable domain are named the "anti-node" and the "node", respectively. The oscillation equations of HRG have two nodes and two anti-nodes in the secondary resonance. Therefore, an HRG can be modeled by a damper (spring damping) and unbalanced mass exchange equations. The Isoelastic errors cause frequency fragmentation and inadequate damping, resulting in an undesirable quality factor (Q). As a result, these issues are important that can lead to errors in HRG performance.

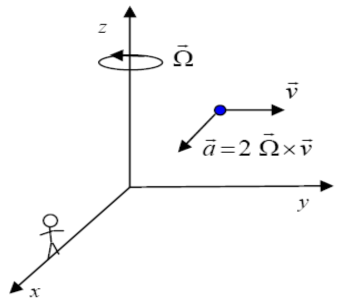

Fig. 1: Understanding the Coriolis force effect.

The location of the maximum domain and the location of the non-portable domain are named the "anti-node" and the "node", respectively. The oscillation equations of HRG have two nodes and two anti-nodes in the secondary resonance. Therefore, an HRG can be modeled by a damper (spring damping) and unbalanced mass exchange equations. The Isoelastic errors cause frequency fragmentation and inadequate damping, resulting in an undesirable quality factor (Q). As a result, these issues are important that can lead to errors in HRG performance.

Two-Dimensional Formulation

The general relations and equations governing the dynamical fluctuations of an HRG and frequency coupling are formulated in equation 2:

$$\begin{bmatrix}\ddot{x}\\ \ddot{y}\end{bmatrix} + \begin{bmatrix}C_{11} & C_{12} - 2k\Omega\\ C_{21} + 2k\Omega & C_{22}\end{bmatrix}\begin{bmatrix}\dot{x}\\ \dot{y}\end{bmatrix} + \begin{bmatrix}K_{11} & K_{12}\\ K_{21} & K_{22}\end{bmatrix}\begin{bmatrix}x\\ y\end{bmatrix} = \begin{bmatrix}f_x\\ f_y\end{bmatrix} \tag{2}$$

where ω is the mean resonance frequency, and K is also the Brain coefficient, which is about 0.3. Other parameters of equation 2 are introduced in equations 3.

$$\begin{aligned}
C_{11} &= \frac{2}{\tau} + \Delta\left(\frac{1}{\tau}\right)\cos(2\theta_\tau)\\
C_{12} &= C_{21} = \Delta\left(\frac{1}{\tau}\right)\sin(2\theta_\tau)\\
C_{22} &= \frac{2}{\tau} - \Delta\left(\frac{1}{\tau}\right)\cos(2\theta_\tau)\\
\omega\Delta\omega &= \frac{\omega_1^2 - \omega_2^2}{2}\\
\Delta\left(\frac{1}{\tau}\right) &= \frac{1}{\tau_1} - \frac{1}{\tau_2}\\
\omega^2 &= \frac{\omega_1^2 + \omega_2^2}{2}\\
\frac{1}{\tau} &= \frac{1}{2}\left(\frac{1}{\tau_1} + \frac{1}{\tau_2}\right)\\
K_{11} &= \omega^2 - \omega\Delta\omega\cos(2\theta_\omega)\\
K_{12} &= K_{21} = -\omega\Delta\omega\sin(2\theta_\omega)\\
K_{22} &= \omega^2 + \omega\Delta\omega\cos(2\theta_\omega)
\end{aligned} \tag{3}$$

In the above formulations, θ_ω is the angle of imbalance between the x-axis and the main axis of the resonance, and θ_τ is the angle between the x-axis and the main axis of the linear damper. To calculate the nominal amplitude and time constant of each axis, it can be assumed initially that the frequency coupling does not exist due to the lack of matching between the damping and unbalanced mass equations. Also, the angular velocity of the input force is not considered. Now, the oscillation characteristic for each axis is given in the form of equation 4.

$$\ddot{x} + \frac{2}{\tau_n}\dot{x} + \omega^2 x = f_x = \frac{f}{m_n} \tag{4}$$
$$subject\ to: x(0) = \dot{x}(0) = 0$$

In this regard, m_n is a modal mass, and can be written to calculate the nominative time constant:

$$\tau_n = \frac{2Q}{\omega} \tag{5}$$

Formerly, the driving force that is applied continuously to the model is equal to:

$$f(t) = \frac{df}{dv}v_c(t) \tag{6}$$

In which, df/dv is the variation of the control force per unit of voltage. Also, the control voltage $v_c(t)$ is expressed using equation 7.

$$v_c(t) = \bar{v}_c\cos(\omega t) \tag{7}$$

Now, using the available data, if equation 6 is solved by the Euler method, it is obtained:

$$x(t) = f_0\frac{Q}{m_n\omega^2}\left(\frac{\sin(\omega t)}{-\frac{1}{\sqrt{1-\left(\frac{1}{2Q}\right)^2}}e^{-\frac{\omega}{2Q}t}\sin(\omega_d t)}\right) \tag{8}$$

In the above relation, f_0 is equal to:

$$f_0 = \frac{dC}{dx} V_B \bar{v}_c \tag{9}$$

V_B is the bias voltage, and dC/dx also represents the variation of the capacitance available based on the variation of the location. We show the relation between the frequencies ω_d and ω with relation 10:

$$\omega_d = \omega \sqrt{1 - \left(\frac{1}{2Q}\right)^2} \tag{10}$$

Therefore, if a large numerical quality coefficient is assumed, $\omega_d = \omega$, consequently, the resulting relation for x(t) will be rewritten as in equation 11 and the modeling is completed.

$$x(t) = f_0 \frac{Q}{m_n \omega^2} \sin(\omega t) \left(\frac{-1}{\sqrt{1 - \left(\frac{1}{2Q}\right)^2}} e^{-\frac{\omega}{2Q} t} \right) \tag{11}$$

After simplifying this convolution integral, the resonator displacement response of relations 13 and 14 can be calculated. If the control force applied is not continuous, $f(t)$ will be in the form of formulation 12. Now, to calculate the system response in the time, domain we have $x(t) = f(t) * h(t)$.

$$f(t) = \begin{cases} \frac{df}{dv} V_B\, \bar{v}_c \cos(\omega t) \;\; ; & C_1 T_0 (n-1) < t \le C_2 T_0 + C_1 T_0 (n-1) \;;\; n\epsilon N \to mode\ 1 \\ 0 \;\; ; & C_2 T_0 + C_1 T_0 (n-1) < t \le C_2 T_0 n \;;\; n\epsilon N \to mode\ 2 \end{cases} \tag{12}$$

$$x(t) = \frac{f_0}{m_n \omega_d} \frac{1}{\left(\frac{\omega}{2Q}\right)^2 + 4\omega^2} \left\{ \sum_{k=1}^{n-1} e^{\frac{nC_1(k-1)}{Q}} \left(e^{\frac{2\pi C_2 - \omega t}{2Q}} - e^{-\frac{\omega t}{2Q}} \right) \times p(t) + q(t) \right\} \to mode\ 1$$

$$x(t) = \frac{f_0}{m_n \omega_d} \frac{1}{\left(\frac{\omega}{2Q}\right)^2 + 4\omega^2} \left\{ \sum_{k=1}^{n-1} e^{\frac{nC_1(k-1)}{Q}} \left(e^{\frac{2\pi C_2 - \omega t}{2Q}} - e^{-\frac{\omega t}{2Q}} \right) \times p(t) \right\} \to mode\ 2 \tag{13}$$

$$p(t) = \left(\frac{\omega}{2Q} + 4\omega Q\right) \sin(\omega_d t) + \omega \cos(\omega_d t)$$

$$q(t) = \left[(4\omega Q \sin(\omega t) + \omega \cos(\omega t)) \left(1 - e^{\frac{2\pi C_1 (n-1) - \omega t}{2Q}}\right) - \frac{\omega}{2Q} \sin(\omega t)\, e^{\frac{2\pi C_1 (n-1) - \omega t}{2Q}} \right] \tag{14}$$

3D Analysis and Finite Element of HRG Vibration

Suppose an HRG is available in spherical coordinates in accordance with Fig. 2. We consider the constants E, ρ, and μ, respectively, of the Young's modulus coefficient, the air density, and the Poisson rate. R and h are also the radius and thickness of the resonator, correspondingly. Therefore, the displacement vector of the resonator is shown in equation 15:

$$\vec{V} = u\, \overrightarrow{a_R} + v\, \overrightarrow{a_\theta} + w\, \overrightarrow{a_\varphi} \tag{15}$$

where u, v, and w are the displacements in the coordinates of spherical coordinates with the vectors R, θ and φ.

If we combine the Coriolis force variations with the acceleration equations, the frequency of different HRG modes is obtained by using equation 16:

$$\omega = \frac{n(n^2-1)}{r^2} \sqrt{\frac{E \,.\, I(n,h)}{3(1+\mu)\rho J(n,h)}} \tag{16}$$

In equation 16, ω is the frequency of different excitation modes of n. We also have:

$$I(n,h) = \int_{\varphi 0}^{\varphi f} \frac{\tan^{2n}\left(\frac{\varphi}{2}\right)}{\sin^3(\varphi)} h^3 d\varphi \tag{17}$$

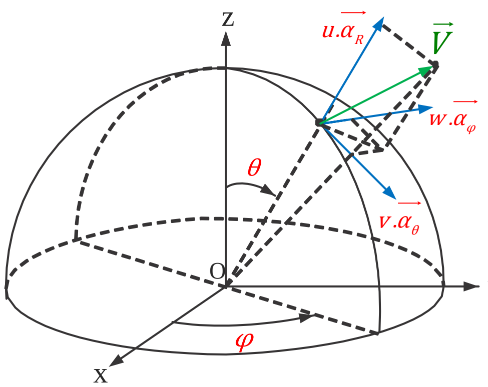

Fig. 2: An HRG depicted in spherical coordinates.

$$J(n,h) = \int_{\varphi 0}^{\varphi f} \begin{matrix} (n^2 + 1 + \sin^2(\varphi) + 2n\cos(\varphi)) \\ * \sin(\varphi) \tan^{2n}\left(\frac{\varphi}{2}\right) h\, d\varphi \end{matrix} \tag{18}$$

If the vector vectors and spherical coordinate parameters are depicted in Fig. 2, then Fig. 3 will be obtained. Afterward, the equations governing this resonator in a three-dimensional spherical device are:

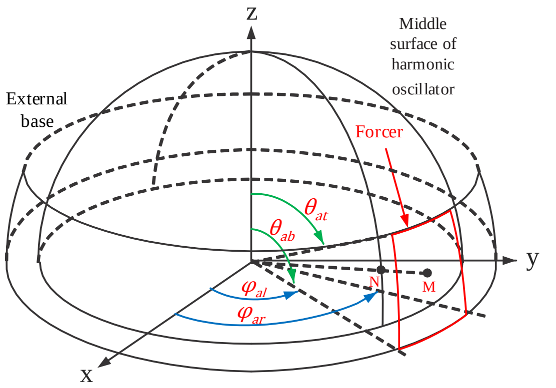

Fig. 3: An HRG in spherical coordinates with an actuator.

$$D\left(\begin{array}{c}\frac{\partial^3\omega}{\partial\theta^3}+\frac{\mu}{\sin(\theta)^2}\frac{\partial^3\omega}{\partial\theta\partial\varphi^2}+\frac{\cos(\theta)}{\sin(\theta)}\frac{\partial^2\omega}{\partial\theta^2}\\ -\frac{\cos(\theta)\,(1+\mu)}{\sin(\theta)^2}\frac{\partial^2\omega}{\partial\varphi^2}+\frac{\sin(\theta)^2-\cos(\theta)^2}{\sin(\theta)^3}\frac{\partial\,\omega}{\partial\theta}\end{array}\right) \tag{19}$$

$$+D_1\left(\frac{1}{\sin(\theta)^2}\frac{\partial^3\omega}{\partial\theta\partial\varphi^2}-\frac{\cos(\theta)}{\sin(\theta)^3}\frac{\partial^2\omega}{\partial\varphi^2}\right)=R^4X$$

$$D\left(\begin{array}{c}\frac{\partial^3\omega}{\partial\theta^3}\frac{1}{sin(\theta)^3}+\frac{\mu}{sin(\theta)}\frac{\partial^3\omega}{\partial\theta^2\partial\varphi}+\frac{cos(\theta)}{sin(\theta)^2}\frac{\partial^2\omega}{\partial\theta\,\partial\varphi}\\ +\frac{\cos(\theta)\,(1+\mu)}{\sin(\theta)^2}\frac{\partial\,\omega}{\partial\varphi}\end{array}\right) \tag{20}$$

$$+D_1\left(\frac{1}{\sin(\theta)}\frac{\partial^3\omega}{\partial\theta^2\partial\varphi}+\frac{1}{\sin(\theta)^3}\frac{\partial\,\omega}{\partial\varphi}\right)=R^4Y$$

$$D\left(\begin{array}{c}\frac{\partial^4\omega}{\partial\theta^4}+\frac{1}{sin(\theta)^3}\frac{\partial^4\omega}{\partial\varphi^4}+\frac{2\mu}{\sin(\theta)^2}\frac{\partial^4\omega}{\partial\theta^2\partial\varphi^2}\\ +2\mathrm{tg}(\theta)\frac{\partial^3\omega}{\partial\theta^3}-\frac{2\mu\cos(\theta)}{\sin(\theta)^3}\frac{\partial^3\omega}{\partial\theta\partial\varphi^2}-\frac{1}{tg(\theta)^2}\frac{\partial^2\omega}{\partial\theta^2}\\ \frac{2(1+\mu)}{\sin(\theta)^4}\frac{\partial^2\omega}{\partial\varphi^2}+\left(\frac{2\cos(\theta)}{\sin(\theta)}+\frac{\cos(\theta)}{\sin(\theta)^3}\right)\frac{\partial\,\omega}{\partial\theta}\end{array}\right) \tag{21}$$

$$+D_1\left(\begin{array}{c}\frac{2}{sin(\theta)^2}\frac{\partial^4\omega}{\partial\theta^2\partial\varphi^2}-\frac{2cos(\theta)}{sin(\theta)^3}\frac{\partial^3\,\omega}{\partial\theta\,\partial\varphi^2}\\ \frac{2}{\sin(\theta)^4}\frac{\partial^2\omega}{\partial\varphi^2}\end{array}\right)=R^4Z$$

In the above relations, R is the radius of the circle and to calculate other values, we have:

$$D=\frac{2Eh^3}{3(1-\mu^2)} \qquad D_1=\frac{2Eh^3}{3(1+\mu^2)} \tag{22}$$

By solving the above equations through combining MATLAB and COMSOL software, the frequency of vibrations and sensor displacements sensed will be calculated and analyzed.

Two-Dimensional Simulation

Initially, the characteristics of the HRG stimulation system are presented in Table 2. This device is then stimulated by the continuous and discrete forces analyzed in the previous section to formulate them to obtain the maximum displacement and its maximum extent. Figures 4 and 5 represent the displacement of the HRG resonator and its maximum range in continuous mode, respectively. Figures 6 and 7 also illustrate the same changes at the time of applying the discontinuous control force. Comparisons show that with time increasing, the displacement growths from zero to 1. 5 pm for continuous mode and from zero to 6 pm for the discrete force input. Accordingly, the maximum resonator amplitude in the discrete mode is less than what is observed in continuous force, consequently, it follows from 12 to 15 that in the continuous mode, the maximum amplitude is 4.9 µm and in the discrete mode will be 0.97 micrometers. Fig. 9 represents the displacement and the resonance frequencies of the second and third modes obtained from simulations. These gyro shapes indicate the resonator edge indents which cause the pick-off electrodes to sense the derived voltage as shown in Fig. 11. The voltage will have high variations around resonance frequencies, used to determine the changing in position and vibration. The resonance frequencies and total displacement of fourth and fifth modes are shown in Fig. 10, too.

Table 2: Specification of HRG stimulation system

Parameters	Value
ω	$\boldsymbol{7\ kHz \times 2\pi \frac{rad}{s}}$
Q	$\boldsymbol{7 \times 10^6}$
m_n	$\boldsymbol{0.85 \times 10^{-3}\ kg}$
$\frac{df}{dv}$	$\boldsymbol{2.78 \times 10^{-6}\ \frac{N}{V}}$
V_B	$\boldsymbol{200\ V}$
$\bar{v}_c$	$\boldsymbol{420\ mV}$
$\frac{dC}{dx}$	$\boldsymbol{13.9 \times 10^{-9}\ \frac{F}{m}}$

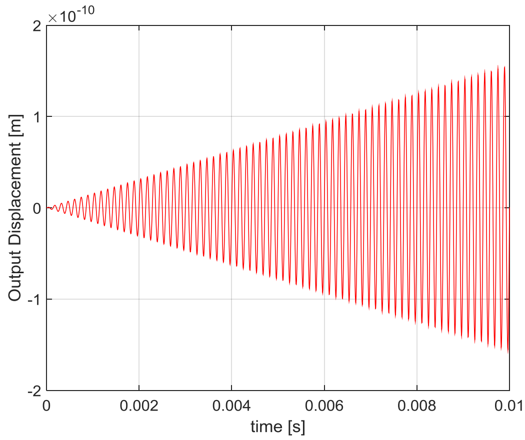

Fig. 4: The output displacement in continuous mode.

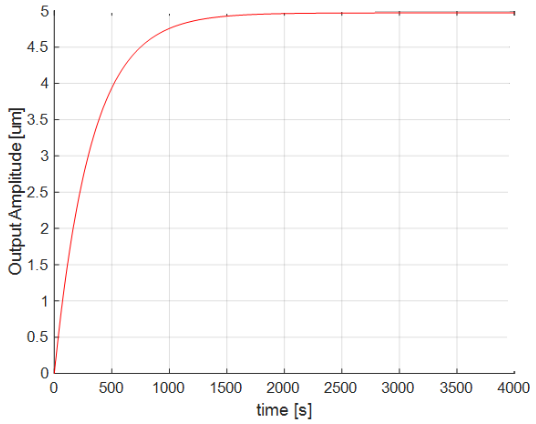

Fig. 5: Maximum amplitude in continuous force mode.

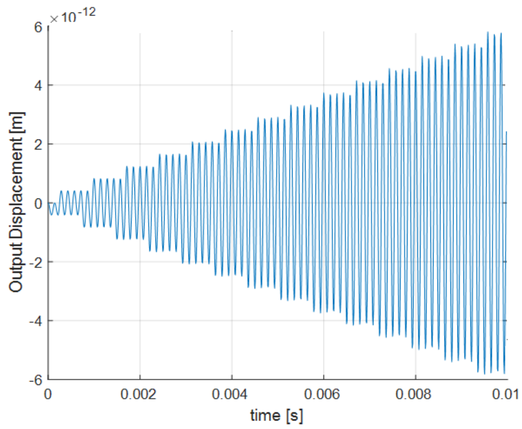

Fig. 6: The output displacement in discontinuous mode.

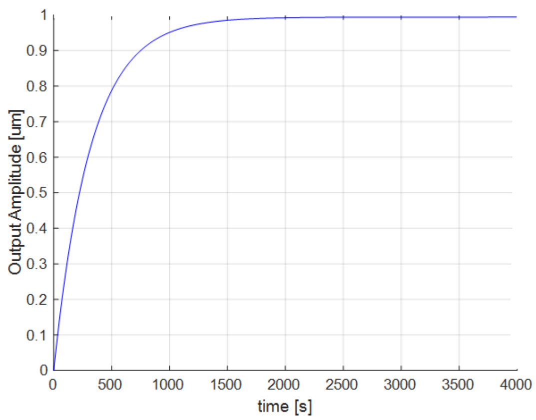

Fig. 7: Maximum amplitude in discontinuous force mode.

3D Sensitivity Analysis

Currently, a HRG specimen with r = 12.5 mm, h = 0.8 mm, d = 2.5 mm, L = 39 mm and ρ = 2651 is shown in Fig. 8. The following tables represent the frequency of different excitation modes by using relationships 16 to 18, as well as using simulations in the COMSOL software. In this section, the frequency of excitation and displacement of the HRG resonator is investigated in various modes and the results are presented in Table 3. This table shows the frequency of HRG stimulation using software and equations 16 to 18. Then, the finite element image of each mode simulated in the Comcast software is depicted.

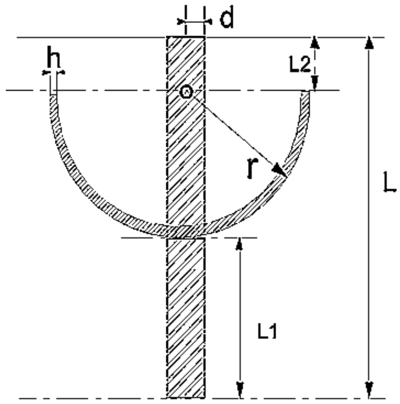

Fig. 8: View of a sample HRG.

Table 3: Comparison of calculated and measured frequencies

Modes	Calculated frequency (Hz)	Measured frequency (Hz)
Mode 2	6899	6903
Mode 3	17301	17310
Mode 4	30427	30434
Mode 5	37281	37095

A. Movement and excitation frequency in various modes

At this platform, the frequency of excitation must be calculated from the instantaneous voltage variation. Therefore, a 2-volt direct-current voltage is applied to the feeders. Then, the voltage sensed by the pixels is visible in Fig. 10. It is then observed that the signal voltages mutate in the vicinity of the frequency of natural HRGs, and this can be verified by the accuracy of the formulation and model.

B. Sensitivity analysis

In this section, the effect of changes in the materials, environment and geometric characteristics of HRG on the stimulated frequency and resonance are evaluated. Given that, in all cases, the sensed voltage is also measured, the maximum mutation in the calculated voltages seems to have the greatest chance of exploitation in that case.

The basic HRG mode is the same as what we have shown in Fig. 8 with these specifications.

At this stage, the radius, the thickness of the resonator, the length and radius of the base, the density of the environment, etc. are changed in the valid range, and the frequency of the various modes will be extracted.

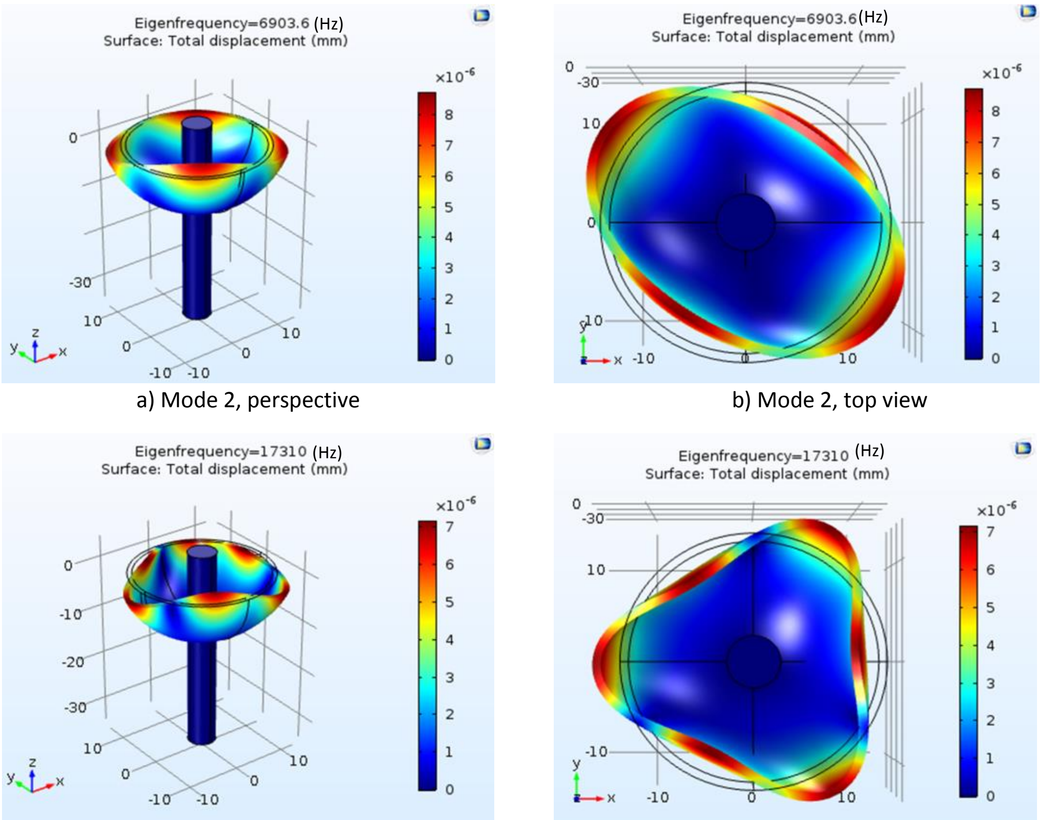

a) Mode 2, perspective b) Mode 2, top view

c) Mode 3, perspective d) Mode 3, top view

Fig. 9: Displacement and frequency of stimulation of the second and third modes.

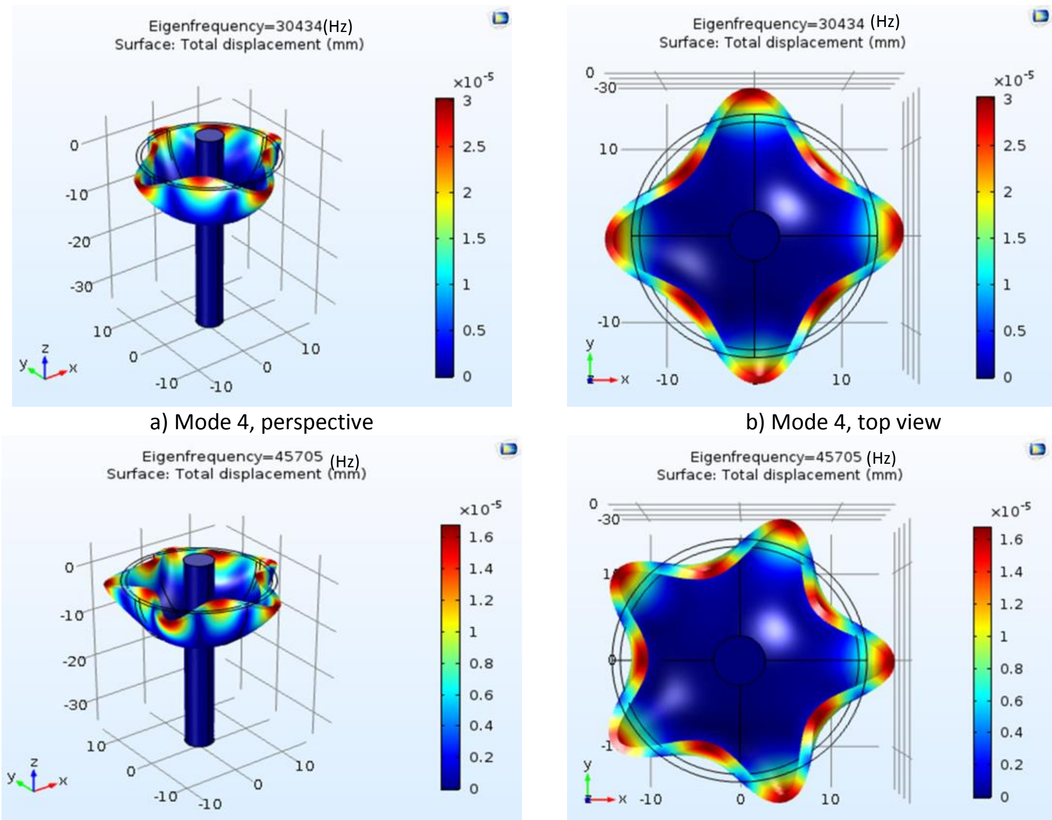

a) Mode 4, perspective b) Mode 4, top view

c) Mode 5, perspective d) Mode 5, top view

Fig. 10: Displacement and frequency of stimulation of the fourth and fifth modes.

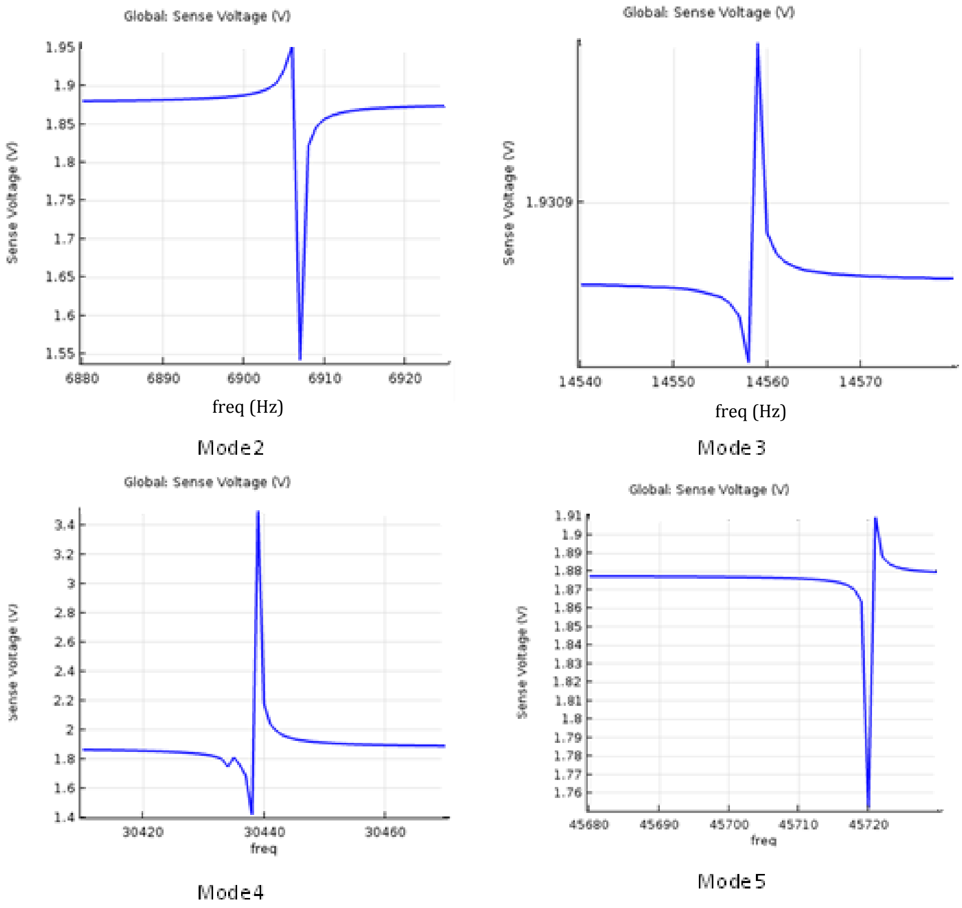

Fig. 11: The sensed voltage diagram around the natural frequencies of the HRG resonator.

I) Sensitivity analysis of radius changes

Given the proposed formulations to calculate the normal HRG frequencies, it can be concluded that the frequency, with the square of the radius, will have a nonlinear and inverse relation. It is noticeable that as the radius increases, the natural frequencies of the various modes decrease. This is due to the increase in the time duration (period) of the wave reaching the end of the resonator shell and its return, which is quite normal.

II) Sensitivity analysis of resonator thickness variations

The base thickness is 0.8 mm. With variations in the thickness of the resonator, the frequency of different modes is measured and recorded in Table 5. As it is seen, increasing the thickness of the resonator increases the excitation frequency, and this is due to the high energy to overcome the fluctuation of the HRG shell.

III) Sensitivity analysis of radius changes

In this section, the radius of the base of the resonator is changed and the resonance frequencies of HRG are recorded in Table 6. Since the sensor base does not have a colorful role in the resonance of the hemisphere, it is expected that it does not have much effect on the excitation frequency.

Comcast software output for calculating the frequency of stimulation of various modes is presented in Table 6.

IV) Sensitivity analysis of sensor base length variations

In this section, the base length is increased by 39 and 44 mm, and the stimulation frequencies are listed in Table 7. Due to the HRG topology, the base length is not expected to affect the frequency of excitation.

V) Sensitivity analysis of density

In this section, by changing the density of the environment from [kg/m^3] 2000 to [kg/m^3] 3000, we can measure resonant frequency variations. According to equation 17, it can be concluded that a decreasing process occurs at the natural frequencies of the system.

Table 4: Sensitivity analysis of radius changes

r [mm]	Frequency (Hz) at n=2	Frequency (Hz) at n=3	Frequency (Hz) at n=4	Frequency (Hz) at n=5
12.5	6903	17310	30434	45705
14.5	5115	12882	23017	34672
16.5	3948	10054	18028	22728

Table 5: Sensitivity analysis of resonator thickness

h [mm]	Frequency (Hz) at n=2	Frequency (Hz) at n=3	Frequency (Hz) at n=4	Frequency (Hz) at n=5
0.6	5233	13151	23586	35628
0.8	6903	17310	30434	45705
1	8552	20930	37107	55628

Table 6: Sensitivity analysis of base resonator radius

d [mm]	Frequency (Hz) at n=2	Frequency (Hz) at n=3	Frequency (Hz) at n=4	Frequency (Hz) at n=5
2.5	6903	17310	30434	45705
3	7017	17376	30432	45711
3.5	7210	17374	30438	45717

Table 7: Sensitivity analysis of base length

L [mm]	Frequency (Hz) at n=2	Frequency (Hz) at n=3	Frequency (Hz) at n=4	Frequency (Hz) at n=5
35	6901	17310	30430	45696
39	6903	17311	30434	45705
44	6899	17414	30429	45689

Table 8: Sensitivity analysis of density

Density [kg/m^3]	Frequency (Hz) at n=2	Frequency (Hz) at n=3	Frequency (Hz) at n=4	Frequency (Hz) at n=5
2000	7943	20051	35039	52621
2651	6903	17310	30434	45705
3000	6485	16078	28597	42946

Briefly, it can be noted that the frequency decreases with increasing radius and density of the resonator. This issue is also consistent with the relation of presentation 16. Now, if the resonator thickness is increased, the frequency increases because relation 17 is in the numerator of the fraction having a power of the third *h* and the relation 18 is in the denominator and having the first power *h*.

This suggests that the frequency is approximately proportional to h. By increasing the density of the environment and reducing E, the frequencies will decrease. All simulations prove the credibility of this claim.

Frequency Split Phenomenon

In most sensors, due to the resonator body retaining frame, another frequency near the main frequency of resonator actuation appears in the frequency domain tests, which is referred to as the frequency separation phenomenon.

In a capacitor gyroscope, this frequency should not be confused with the original frequency of the stimulation mode, since it will cause the whole system to be undesirable.

To this end, these frequencies must be identified to distinguish the main modes. COMSOL software extracts this frequency at various HRG stimuli.

In this section, the segregated frequencies in the HRGs discussed in the second mode are analyzed.

This phenomenon can also affect CRGs. Fig. 12 depicts the frequency separation in three important gyroscope samples.

Conclusion

In this paper, a novel formulation for two-dimensional and three-dimensional analysis of vibrational corneal-based gyroscopes with capacitive excitation was presented.

These frameworks validated with simulation results are capable to be utilized on cylindrical or bell-shaped gyroscopes.

The resonance frequencies on different modes obtained by COMSOL software represent the various design procedures on the corresponding applications. The pick-offs and forcers are considered to be made of hard iron to prevent corrosion against changing in the electric and magnetic fields applied to the gyroscope. Sensitivity analysis of environment density represents that, the denser atmosphere results in low resonance frequency, while the variation of base length of the gyro, will not influence the frequencies that much.

The resonator radius growing up will increase the resonance frequencies in each mode, either the resonator thickness increment has the same consequence.

The simulation results showed that the voltage will have high variations around resonance frequencies, which is used to be sensed by pick-off electrodes to determine the changing in position and vibration.

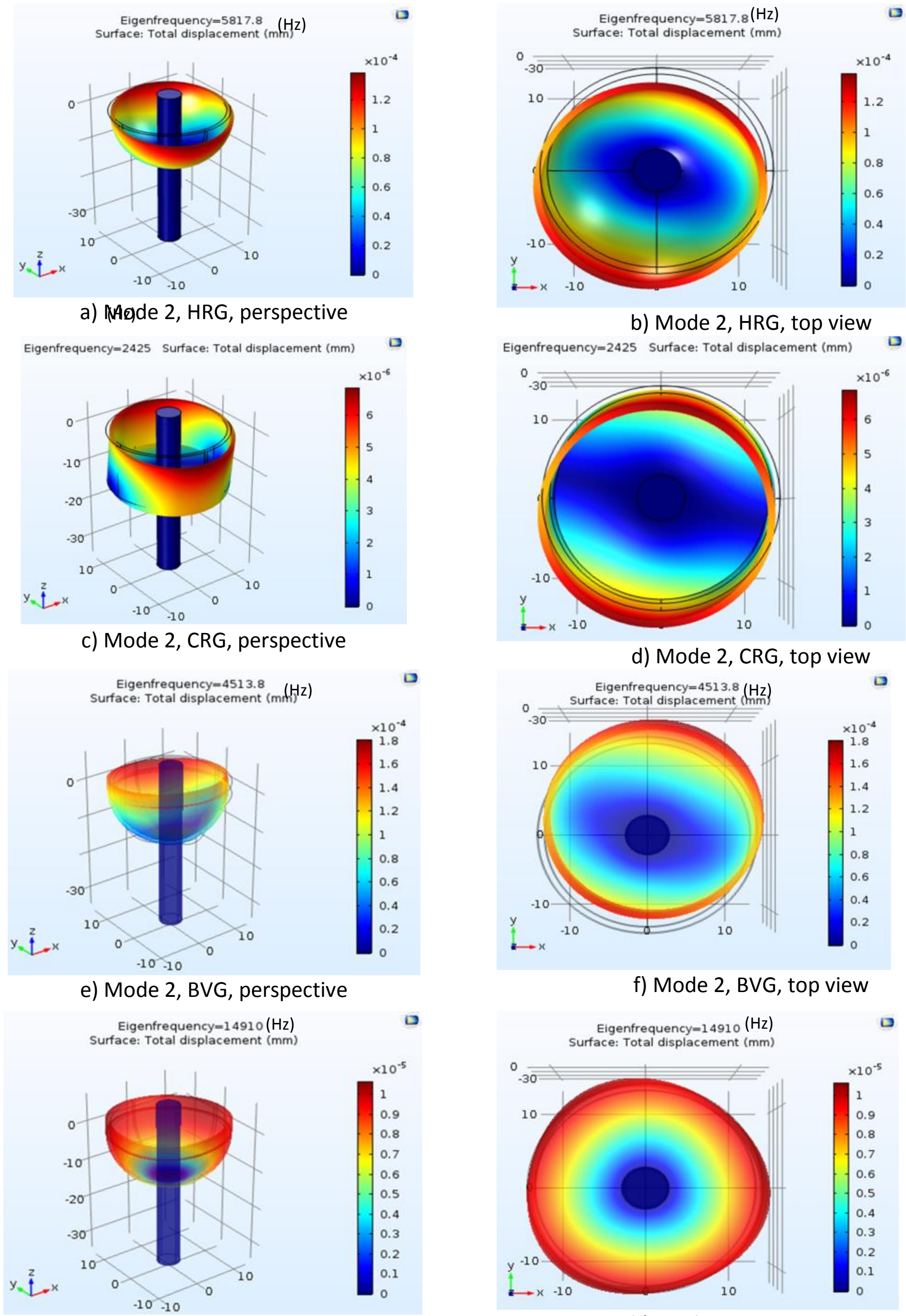

a) Mode 2, HRG, perspective
b) Mode 2, HRG, top view
c) Mode 2, CRG, perspective
d) Mode 2, CRG, top view
e) Mode 2, BVG, perspective
f) Mode 2, BVG, top view
g) Mode 3, BVG, perspective
h) Mode 3, BVG, top view

Fig. 12: Frequency split separation in different modes of Coriolis gyroscopes.

References

[1] M. Ghaderi, V. Tabataba Vakili, M. Sheikhan, "STCS-GAF: spatio-temporal compressive sensing in wireless sensor networks- A GAF-based approach," Journal of Electrical and Computer Engineering Innovations, 6(2): 153-166, 2018.

[2] S. Ranjbaran, A. Roudbari, S. Ebadollahi, "A simple and fast method for field calibration of triaxial gyroscope by using accelerometer," Journal of Electrical and Computer Engineering Innovations, 6(1): 1-6, 2018.

[3] S. Shams Shamsabad Farahani, "Congestion control approaches applied to wireless sensor networks: A survey," Journal of Electrical and Computer Engineering Innovations, 6(2): 125-144, 2018.

[4] P. Halvaee, M. Beigi, "Room temperature methanol sensor based on ferrite cobalt (cofe2o4) porous nanoparticles," Journal of Electrical and Computer Engineering Innovations, 6(2): 209-216, 2018.

[5] M. Shaveisi, A. Rezaei, "Performance analysis of reversible sequential circuits based on carbon nanotube field effect transistors (CNTFETs)," Journal of Electrical and Computer Engineering Innovations, 6(2): 167-178, 2018.

[6] Z. C. Feng, K. Gore, "Dynamic characteristics of vibratory gyroscopes," IEEE Sensors Journal, 4(1): 80-84, 2004.

[7] G. He, Z. Geng, "Dynamics and robust control of an under-actuated torsional vibratory gyroscope actuated by electrostatic

actuator," IEEE/ASME Transactions on Mechatronics, 20(4): 1725-1733, 2015.
[8] Y. Dong, M. Kraft, W. Redman-White, "Micro-machined vibratory gyroscopes controlled by a high-order band-pass sigma-delta modulator," IEEE Sensors Journal, 7(1): 59-69, 2007.
[9] S. A. Zotov, A. A. Trusov, A. M. Shkel, "Three-dimensional spherical shell resonator gyroscope fabricated using wafer-scale glassblowing," Journal of Micro Electromechanical Systems, 21(3): 509-510, 2012.
[10] E. Tatar, T. Mukherjee, G. K. Fedder, "Stress effects and compensation of bias drift in a mems vibratory-rate gyroscope," Journal of Micro Electromechanical Systems, 26(3): 569-579, 2017.
[11] J. Fei, "Robust adaptive vibration tracking control for a micro-electro-mechanical systems vibratory gyroscope with bound estimation," IET Control Theory & Applications, 4(6): 1019-1026, 2010.
[12] Y. Lu, X. Wu, W. Zhang, W. Chen, F. Cui, W. Liu, "Optimal special vibration used as reference vibration of vibratory gyroscopes," Electronics Letters, 46(2): 155-156, 2010.
[13] S. Sung, W. Sung, C. Kim, S. Yun, Y. J. Lee, "On the mode-matched control of mems vibratory gyroscope via phase-domain analysis and design," IEEE/ASME Transactions on Mechatronics, 14(4): 446-455, 2009.
[14] P. Lynch, "In retrospect replication of Foucault's pendulum experiment in Dublin,".
[15] W. H. Quick, "Theory of the vibrating string as an angular motion sensor," Journal of Applied Mechanics, 31(3): 523-534, 1964.
[16] T. Tognola, "Magneto-electric motion detecting transducer," U.S. Patentb 3,129,347. 14,. 1964.
[17] J. Cui, Z. Guo, Q. Zhao, Z. Yang, Y. Hao, G. Yan, "Force rebalance controller synthesis for a micro-machined vibratory gyroscope based on sensitivity margin specifications," Journal of Micro-Electromechanical Systems, 20(6): 1382-1394,. 2011.
[18] E. Song, S. Kang, H. Kim, Y. Kim, J. An, C. Baek, "Wafer-level fabrication of a fused-quartz double-ended tuning fork resonator oscillator using quartz-on-quartz direct bonding," IEEE Electron Device Letters, 34(5): 692-694, 2013.
[19] M. F. Zaman, A. Sharma, Z. Hao, F. Ayazi, "A mode-matched silicon-yaw tuning-fork gyroscope with subdegree-per-hour Allan deviation bias instability," Journal of Micro-Electromechanical Systems, 17(6): 1526-1536, 2008.
[20] S. A. Zotov, B. R. Simon, I. P. Prikhodko, A. A. Trusov, A. M. Shkel, "Quality factor maximization through dynamic balancing of tuning fork resonator," IEEE Sensors Journal, 14(8): 2706-2714, 2014.
[21] D. R. Myers, R. G. Azevedo, L. Chen, M. Mehregany, A. P. Pisano, "Passive substrate temperature compensation of doubly anchored double-ended tuning forks," Journal of Micro-Electromechanical Systems, 21(6): 1321-1328, 2012.
[22] K. W. Leung, C. K. Leung, "Wideband dielectric resonator antenna excited by cavity-backed circular aperture with microstrip tuning fork," Electronics Letters, 39(14): 1033-1035, 2003.
[23] C. Yang, H. Li, "Digital control system for the mems tuning fork gyroscope based on synchronous integral demodulator," IEEE Sensors Journal, 15(10): 5755-5764, 2015.
[24] P. Shao, C. L. Mayberry, X. Gao, V. Tavassoli, F. Ayazi, "A poly-silicon micro-hemispherical resonating gyroscope," Journal of Micro-Electromechanical Systems, 23(4): 762-764, 2014.
[25] J. W. Song, H. Song, Y. J. Lee, C. G. Park, S. Sung, "Design of oscillation control loop with coarse-precision mode transition for solid-state resonant gyroscope," IEEE Sensors Journal, 16(6): 1730-1742, 2016.
[26] C. Dai, D. Pi, Z. Fang, H. Peng, "A novel long-term prediction model for hemispherical resonator gyroscope's drift data," IEEE Sensors Journal, 14(6): 1886-1897, 2014.
[27] A. Darvishian, B. Shiari, J. Y. Cho, T. Nagourney, K. Najafi, "Anchor loss in hemispherical shell resonators," Journal of Micro-Electromechanical Systems, 26(1): 51-66, 2017.
[28] Z. Liu, W. Zhang, F. Cui, J. Tang, Y. Zhang, "Fabrication and characterization of micro-scale hemispherical shell resonator with diamond electrodes on the Si substrate," Micro & Nano Letters, 14(6): 674-677, 2019.

Biographies

Reza Sedaghati was born in Kazeroon, Iran, in 1983. He received his M.Sc. degree in Electrical Engineering in 2009, and a Ph.D. degree in Electrical Engineering from Lorestan University in 2019. Currently, he is an Assistant Professor at the Department of Electrical Engineering, Beyza Branch, Islamic Azad University, Beyza, Iran. His research interests include renewable energies, optimization, FACTS devices, and power system dynamics.

Mehrdad Mahmoudian was born in Fasa, Iran, in 1990. He received his B.Sc. degree in Electrical Engineering from Shahid Bahonar University, Kerman, Iran, and M.Sc. degree in Electrical Engineering from Iran University of Science and Technology (IUST), Tehran Iran, in 2012 and 2014, respectively. Currently, he is working towards a Ph.D. degree in Electrical Engineering at Shiraz University of Technology, Shiraz, Iran. His research interests include Coriolis Gyros, DC/DC Converters, DC/AC Inverters, Energy Conversion, and Photovoltaic Power System.

Copyrights
©2019 The author(s). This is an open access article distributed under the terms of the Creative Commons Attribution (CC BY 4.0), which permits unrestricted use, distribution, and reproduction in any medium, as long as the original authors and source are cited. No permission is required from the authors or the publishers.

How to cite this paper:
R. Sedaghati, M. Mahmoudian, "Hemispherical vibratory gyroscope performance evaluation and sensitivity analysis with capacitive excitation," Journal of Electrical and Computer Engineering Innovations, 7(1): 47-58, 2019.

DOI: 10.22061/JECEI.2019.5565.239

URL: http://jecei.sru.ac.ir/article_1170.html